RSC Advances

PAPER

View Article Online
View Journal | View Issue

Cite this: *RSC Adv.*, 2023, **13**, 32023

One-dimensional $H_2V_3O_8$ nanorods and two-dimensional lamellar MXene composites as efficient cathode materials for aqueous rechargeable zinc ion batteries†

Wenyuan Duan, [a] Shenghua Chen,[b] Yanlin Li, *[b] Shaoquan Chen[a] and Yuzhen Zhao *[a]

The energy crisis is a the worldwide problem which needs humans to solve immediately. To solve this problem, it is necessary to develop energy storage batteries. It is worth mentioning the aqueous rechargeable zinc ion batteries (ARZBs) which have some advantages, such as low cost, good safety and no need for an organic electrolyte as in the traditional lithium-ion batteries. However, it is still a challenge to find suitable and reliable electrode materials. In this work, as-prepared $H_2V_3O_8$ nanorods and MXene composites are used as cathode materials in ARZBs which were designed well using a hydrothermal method after optimizing the reaction time. The results showed that $H_2V_3O_8$/MXene ARZBs could provide a good transport path for zinc ions, which were based on special 1D $H_2V_3O_8$ nanorods and 2D multi-layered MXene materials, which exhibited an outstanding initial specific discharge capacity of 373 mA h g^{-1} at 200 mA g^{-1}, good rate capability and a long lifecycle with only 15.8% capacity decay at 500 mA g^{-1} after 5000 cycles. The $H_2V_3O_8$/MXene composites with a good electrochemical performance bring insight into their promising applications for energy storage batteries. They provided enhanced rate performance and excellent cycling stability, which was ascribed to the multi-step and multi-mode zinc ion insertion/extraction process. This was confirmed by the use of the 1D/2D integrated structure of the $H_2V_3O_8$/MXene composites, which was conductive to zinc ion diffusion.

Received 23rd August 2023
Accepted 17th October 2023

DOI: 10.1039/d3ra05754b

rsc.li/rsc-advances

Introduction

Because of the extensive use of fossil energy, the problem of environmental pollution is becoming more and more serious. A series of policies have been introduced to encourage the use of green energy, especially in China with the actual national conditions of less gas storage and lack of oil. However, some green energy sources, such as wind and solar power, which are subject to variations in natural conditions, are intermittent and uncontrollable. Therefore, there is an urgent demand for energy storage batteries.[1,2] Traditional lithium ion batteries have a high energy density,[3–6] good charging ability, no memory effect and no need for periodic maintenance charge and discharge. Therefore, they are widely used in energy storage devices, such as mobile phones, notebook computers, electric vehicles and so on.

Unfortunately, traditional lithium ion batteries have great problems such as high cost and poor safety due to the use of organic electrolytes.[7,8] Therefore, new aqueous rechargeable batteries have emerged, which can improve the ionic mobility in aqueous solution and have good electrochemical performance in high-rate charge and discharge environments. For example, Meng and co-workers used rational design to create a multi-layer rGO@Mn_2SiO_4@ZIF-8-C using a layer-by-layer assembly method, which ensured the Li-ion transfer kinetics and inhibited Mn_2SiO_4 dissolution during the electrochemical reaction in aqueous rechargeable lithium ion batteries (ARLBs).[9]

It is should be mentioned that compared with the ARLBs, aqueous rechargeable zinc ion batteries (ARZBs) are safer and cheaper because zinc can be stably preserved at room temperature and has abundant reserves.[10,11] Guo and co-workers first reported a new type of ARZB which used an organic pH-buffer containing N heterocyclic compounds as an additive to prevent the formation of Zn dendrites, the hydrogen evolution reaction and anode corrosion.[12] Recently, novel two-dimensional (2D) MXene materials with a typical chemical

[a]*Xi'an Key Laboratory of Advanced Photo-electronics Materials and Energy Conversion Device, Xijing University, Xi'an 710123, China. E-mail: zyz19870226@163.com*
[b]*School of Materials Science and Engineering, Xi'an University of Architecture & Technology, Xi'an 710055, China. E-mail: liyanlin@xauat.edu.cn*

† Electronic supplementary information (ESI) available: Fig. S1: the TEM image of $H_2V_3O_8$ (36 h) nanorods. Fig. S2: the TEM image of MXene. Fig. S3: the SEM image of $H_2V_3O_8$/MXene. Fig. S4: the capacitive and diffusion-controlled contribution $H_2V_3O_8$/MXene composites ARZBs at 2, 4, 8, 10 mV s^{-1}. See DOI: https://doi.org/10.1039/d3ra05754b

formula of $M_{n+1}X_nT_x$ (M represents metals, Ti, Ta, and so on; X represents C, N, and so on; and T represents a terminal group)[13] have attracted researchers' attention due to their nanolaminate microstructure, superior conductivity and high specific surface area,[14] and they are considered to be a promising candidate, as pseudocapacitive materials for energy storage devices.[15] For example, Zn ion supercapacitors were assembled by combining the zinc metal anode and Ti_2CT_x-MXene aerogel as a cathode,[16] which exhibited outstanding charge performance because of the convenient and fast ion transmission caused by the MXene materials. The 2D MXene sheets were grown on $H_2V_3O_8$ nanowires to form an integrated structure, which showed enhanced electrical conductivity, superior rate performance and a long lifespan.[16]

Herein, we first prepared $H_2V_3O_8$ nanorods using a simple hydrothermal method. Different reaction times were tested to obtain the most suitable $H_2V_3O_8$ with good morphology and electrochemical performance. Subsequently, the $H_2V_3O_8$/MXene composites were prepared similarly and used as cathode materials in ARZBs to measure the electrochemical performance. The schematic diagram of the experiment is shown in Fig. 1. The results showed that the $H_2V_3O_8$/MXene composites presented better rate capability and initial specific discharge capacity than the $H_2V_3O_8$ materials. It was also found that the $H_2V_3O_8$/MXene composites exhibited a longer lifecycle and stability. The difference in electrochemical performance of the $H_2V_3O_8$/MXene composites compared with the $H_2V_3O_8$ derived from 2D multi-layered MXene was beneficial for the transportation of ions. Therefore, it is a possible potential solution to be applied in energy storage batteries with high performance requirements.

Experimental

Synthesis of the $H_2V_3O_8$ nanorods

$H_2V_3O_8$ was synthesized by a one-step hydrothermal method. In a typical process, 1.8 mmol of V_2O_5 powder, as the raw material, was dissolved in a deionized water/acetone (32 ml/1 ml) solution with vigorous magnetic stirring for 4 h at room temperature. Then the solution was transferred to a Teflon-lined stainless-steel autoclave (50 ml) and heated at 180 °C for 24 h (H24), 36 h (H36) or 48 h (H48). Finally, the as-obtained products were centrifuged and washed with ethanol and then dried at 50 °C in a vacuum for 12 h to obtain the $H_2V_3O_8$ nanorods.

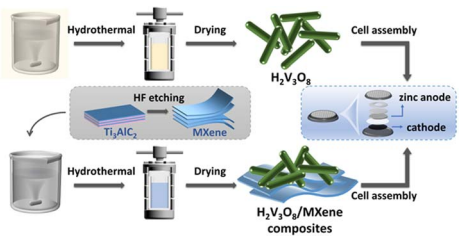

Fig. 1 The schematic diagram of the preparation of $H_2V_3O_8$ and $H_2V_3O_8$/MXene composites, and the cell assembly.

Preparation of MXene

Firstly, Ti_3AlC_2 (1 g) as a precursor material was dispersed in HF (30 ml) with magnetic stirring for 12 h. During the process, the Ti_3AlC_2 powder was slowly added to the HF solution to prevent overheating. As the time of reaction increased, the aluminum was etched off to obtain MXene (Ti_3C_2). Finally, the as-obtained products were centrifuged and washed several times with deionized water and then dried at 50 °C.

Synthesis of the $H_2V_3O_8$/MXene composites

The synthesis was similar to the method used for the $H_2V_3O_8$ nanorods, except that MXene was added to the precursor solution ($H_2V_3O_8$: MXene = 1 g : 38 mg). The products were obtained u a hydrothermal method with heating at 180 °C for 36 h.

Characterization

The phase structure was measured by X-ray diffraction (XRD, D8 Advance A25, Bruker, Germany; CuKα, $\lambda = 0.15418$ nm, 2θ: 0–90°, 5° min^{-1}). The morphology was characterized by field-emission scanning electron microscopy (FESEM, JSM-7000F, Jeol, Japan) at an acceleration voltage of 15.0 kV, and transmission electron microscopy (TEM, HT7800, Jeol, Japan) at 100 kV.

Cell assembly and electrochemical performance testing

The $H_2V_3O_8$ or $H_2V_3O_8$/MXene composites were used as the cathode, and zinc foil as the anode with $Zn(CF_3SO_3)_2$ as the electrolyte. The cathode was made by mixing $H_2V_3O_8$ or the $H_2V_3O_8$/MXene composite powder, acetylene black, and poly(-vinylidene fluoride) (PVDF) in a mass ratio of 7 : 2 : 1. The black slurry obtained after using *N*-methylpyrrolidone (NMP) as a solvent was uniformly mixed using an ultrasonic process for about 2 min. The well-mixed cathode material was coated onto a stainless mesh and then dried in a vacuum. The cathode mass loading was about 3 mg. The anode used was a commercial zinc foil. A glass fiber membrane was chosen as the separator. In this experiment, we used model 2032 button batteries. The electrochemical performance was tested using a Blue Electrical Test System and the cyclic voltammetry (CV) curves were measured using an electrochemical workstation within 0–1.2 V (*vs.* Zn/Zn^{2+}) at 2, 4, 8, 10, 20 mV s^{-1}.

Results and discussion

The XRD patterns of $H_2V_3O_8$ with different reaction times are shown in Fig. 2a, and the strong peaks corresponding to (200), (110), (310), (020), (320), (011), (520) and (002) were indexed to vanadium oxide hydrate (PDF#85-2401). In addition, using the Scherrer equation (eqn (1)), we calculated the crystalline size of $H_2V_3O_8$ with different reaction times. The crystalline sizes were 32.5 nm (H24), 33.7 nm (H36) and 29.4 nm (H48).

$$D = \frac{k\gamma}{B\cos\theta} \quad (1)$$

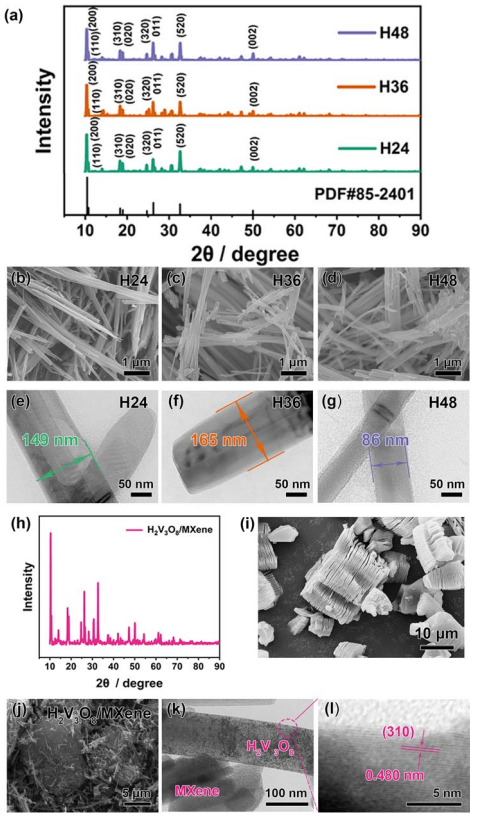

Fig. 2 (a) The XRD patterns of $H_2V_3O_8$ (H24, H36 and H48). (b)–(d) The SEM images of H24, H36 and H48, respectively. (e)–(g) The TEM images of H24, H36 and H48, respectively. (h) The XRD patterns of the $H_2V_3O_8$/MXene composites. (i) The SEM image of MXene. (j) The SEM image of the $H_2V_3O_8$/MXene composites. (k) The TEM image of the $H_2V_3O_8$/MXene composites. (l) The HRTEM of the $H_2V_3O_8$/MXene composites.

There was an obvious difference in the morphology sizes, which is shown in the FESEM and TEM images. From the low-magnification FESEM images in Fig. 2b–d, the as-prepared $H_2V_3O_8$ was a one-dimensional (1D) nanorod. Moreover, the 1D nanorod-like structure was further confirmed from the TEM images in Fig. 2e–g, whose diameters were about 149 nm (H24), 165 nm (H36) and 86 nm (H48). The results showed that the crystalline size affected the rod size of $H_2V_3O_8$. It appears that the diameter of the $H_2V_3O_8$ nanorods increased with the increase in crystalline size. The uniform rod-like structure of H36 is shown in Fig. S1 (ESI).† During the reaction, the $H_2V_3O_8$ nanorods formed and grew as the reaction increased. The $H_2V_3O_8$ nanorods formed gradually when the reaction time was 24 h. Next, the stable structure of the $H_2V_3O_8$ nanorods was obtained within 36 h. Furthermore, as the reaction time continued to increase, the stable structure of the $H_2V_3O_8$ nanorods was destroyed to a certain extent. As a result, H36 presented the better rate capability when compared with the H24 and H48 nanorods. For the $H_2V_3O_8$/MXene composites, the main diffraction peaks were matched with vanadium oxide hydrate (Fig. 2h), but there were no other obvious peaks for MXene, which was probably due to the trace amount of MXene used during the preparation process.

According to a previous study, the MXene is a 2D material with a multiple-layer structure, which is shown in Fig. 2i (the TEM image is shown in Fig. S2, ESI†). In the SEM image (Fig. 2j), the 1D $H_2V_3O_8$ nanorods were deposited and grown on 2D MXene. In Fig. S3 (ESI),† the SEM image further demonstrated the growth of $H_2V_3O_8$ nanorods between the MXene layers. From the high-magnification TEM images in Fig. 2k, it was found that a composite structure was observed with the $H_2V_3O_8$ nanorods and lamellar MXene. A representative HRTEM image in Fig. 2l shows the lattice fringe spacing of 0.480 nm, which corresponded to the (310) plane of $H_2V_3O_8$, which was consistent with the results obtained from the XRD patterns in Fig. 2a and h.

Fig. 3a–c show the typical CV curves of $H_2V_3O_8$ in the voltage range between 0 V and 1.2 V (*vs.* Zn/Zn^{2+}) at scan rates of 2, 4, 8, 10 and 20 mV s^{-1}. On the basis of the CV measurements, H24, H36 and H48 exhibited one pair of significant reversible redox peaks located at about 0.61/0.66/0.70 V (anodic peaks) and 0.38/0.37/0.35 V (cathodic peaks), demonstrating that a significant portion of the capacitance originated from the pseudo capacitance according to the autonomous and reversible redox process.[17] Thus, the $H_2V_3O_8$ cathode showed excellent electrochemical properties.[18–21] These $H_2V_3O_8$ materials had good reversibility because of the contact between the $H_2V_3O_8$ nanorods and the nanorod structure was conducive to charge transport. As a result, the nanorod-like structure of $H_2V_3O_8$ provided a stable structure for zinc ion insertion/extraction.

The electrochemical kinetics of the $H_2V_3O_8$/MXene composites' cathode were further investigated to quantitatively determine the diffusion-controlled and capacitive contributions at different scan rates (2–20 mV s^{-1}).[16] As shown in Fig. 3d, each curve of the $H_2V_3O_8$/MXene composites at different scan rates also presented one main pair of redox peaks located at about 0.74 V (anodic peaks) and 0.43 V (cathodic peaks), which indicated that there was synergistic capacitive behavior and diffusion during the electrochemical reaction of ARZBs based on $H_2V_3O_8$/MXene composites. The curves showed a similar shape but there was some shift in the redox peak, indicating that polarization had occurred during the electrochemical reaction.

Furthermore, the proportion of the capacitive contribution could be quantified using eqn (2):[22]

$$i\,(\mathrm{V}) = k_1\nu + k_2\nu^{1/2} \tag{2}$$

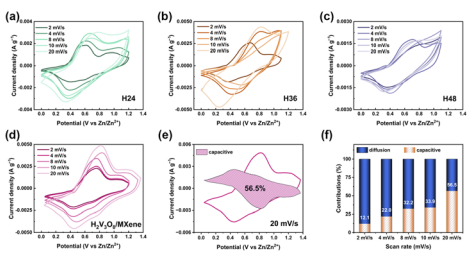

Fig. 3 The CV curves of (a) H24, (b) H36, (c) H48, and (d) the $H_2V_3O_8$/MXene composites, respectively. (e) The capacitive contribution of $H_2V_3O_8$/MXene, and (f) the capacitive contributions at different scan rates.

where i represents the current density (A g^{-1}), $k_1\nu$ represents the capacitive contribution, and $k_2\nu^{1/2}$ represents the diffusion-controlled contribution. Taking the scan rate from 2 to 4, 8, 10 and 20 mV s^{-1}, it was possible to observe that the $H_2V_3O_8$/MXene ARZBs could still keep the shape of the CV curves with a slight shift of the anodic and cathodic peaks, even at a high scan rate of 20 mV s^{-1}, suggesting there was a capacitive-type storage nature and an exceptional rate capability.[17] The capacitive contribution in the $H_2V_3O_8$/MXene composites accounted for 56.5% of the total capacity at a scan rate of 20 mV s^{-1}, which is shown in Fig. 3e. Moreover, with the increase in the scan rate, the capacitive contribution in the $H_2V_3O_8$/MXene composites improved gradually, which can be seen in Fig. 3f, where the capacitive contributions were 12.1%, 22.0%, 32.2%, 33.9% and 56.5%, at 2, 4, 8, 10 and 20 mV s^{-1}, respectively. The corresponding calculation results of the capacitive contribution for other different scan rates (2, 4, 8 and 10 mV s^{-1}) are shown in Fig. S4 (ESI).† Generally, the CV peaks shifted to different degrees due to polarization. In other words, the current value that should correspond to a certain potential would be offset at a larger sweep speed, which leads to the existence of pseudo capacitance. The effect of the scanning rate on pseudo capacitance can be analyzed in three ways: (1) limitations of charge transport processes: the greater the sweep speed is, the greater the rate of charge transfer is, and the larger the pseudo capacitance is. (2) limitations of electrochemical reactions: the diffusion rate and reaction rate of ions are also limited by the electrochemical reactions. When the scanning rate increases, the reaction rate will also increase, and the pseudo capacitance will also increase. (3) Limitations of surface reactions: the contribution of pseudo capacitance is also affected by the electrode surface reaction. As the scanning rate increases, the surface reaction rate and the pseudo capacitance also increase.

The rate capability of $H_2V_3O_8$ and $H_2V_3O_8$/MXene is shown in Fig. 4. For H24, the rate capability was measured by progressively increasing the current density from 200 mA g^{-1}, 500 mA g^{-1}, 800 mA g^{-1}, 1 A g^{-1} to 2 A g^{-1}, then returning it to 200 mA g^{-1}, which is shown in Fig. 4a. As far as it could be seen, H24 presented a lower specific discharge capacity of 304 mA h g^{-1} at 200 mA g^{-1}. However, H36 exhibited a higher specific discharge capacity with 342 mA h g^{-1} at 200 mA g^{-1} (Fig. 4b). The H36 was recycled at 200 mA g^{-1} and retained a specific discharge capacity of 313 mA h g^{-1}, thus, demonstrating a better rate capability. For

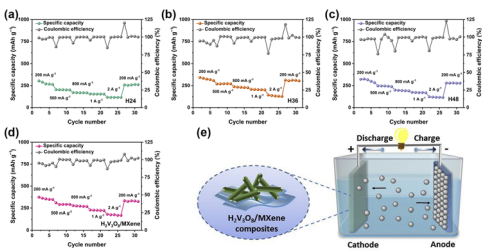

Fig. 4 The rate capability and coulombic efficiency of (a) H24, (b) H36, (c) H48 and (d) $H_2V_3O_8$/MXene composites at current densities of 200, 500, 800, 1000, 2000 and 200 mA g^{-1}. (e) A schematic of the assembly structure of the $H_2V_3O_8$/MXene ARZBs.

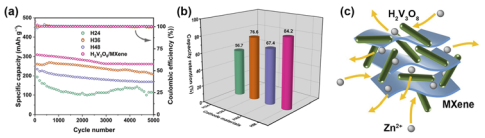

Fig. 5 (a) The cycling stability of $H_2V_3O_8$ and $H_2V_3O_8$/MXene composites at a current density of 500 mA g^{-1}, (b) the capacity retention, and (c) a schematic of the reversible zinc ion insertion/extraction process in the MXene.

H48 shown in Fig. 4c, the specific discharge capacity decreased when compared to H36; it first achieved 322 mA h g^{-1} at 200 mA g^{-1} and then returned to 280 mA h g^{-1}. As for the $H_2V_3O_8$/MXene composites in Fig. 4d, the specific discharge capacity improved greatly when compared to H24, H36 and H48, and reached 373 mA h g^{-1} when the current density was 200 mA g^{-1}. Even though the current density rose to 2 A g^{-1}, the specific discharge capacity could still preserve 169 mA h g^{-1}, which was much higher than that of $H_2V_3O_8$. Furthermore, when the current density was back to 200 mA g^{-1}, the reversible specific capacity of $H_2V_3O_8$/MXene returned to 333 mA h g^{-1} with a recovery ratio of about 89.3%, indicating its excellent electrochemical reversibility. The great rate capability of the $H_2V_3O_8$/MXene composites was attributed to the multiple and complex morphology of the 1D rod-like structure, as well as the 2D lamellar MXene (Fig. 4e), which was more conducive to the penetration and rapid transfer of electrolytes.[23–25]

The cycling performance of the ARZBs was evaluated according by measuring the specific discharge capacity at different numbers of cycles at 500 mA g^{-1} (Fig. 5). The H24 presented a low cycling stability and the discharge capacity of H48 decreased significantly with the increasing cycle number, which is shown in Fig. 5a. For H36, the capacity fluctuated obviously as the cycle number increased. In comparison, the $H_2V_3O_8$/MXene ARZBs showed a high cycling stability at a current density of 500 mA g^{-1} and the capacity retention remained at 84.2% after 5000 cycles, whereas H24, H36 and H48 only remained at 56.7%, 76.6% and 67.4%, respectively, as shown in Fig. 5b. The $H_2V_3O_8$/MXene provided excellent cycling stability, which was superior to that of the as-prepared $H_2V_3O_8$ nanorods. It was accepted that the MXene materials were able to provide high structural stability, an abundance of active sites and an excess of open channels (Fig. 5c), which allowed rapid ion diffusion.[17,26,27] Generally, during the charge and discharge cycles, the dendrites grew on the zinc electrode, and the zinc electrode was corroded by this and dissolved gradually in the electrolyte over a long time, resulting in some inevitable degradation of the capacity.[28–33] Given the reversible insertion/extraction process of the zinc ions,[34–38] the electrochemical performance of the $H_2V_3O_8$/MXene composites improved.

Conclusions

In summary, the $H_2V_3O_8$ nanorods were first prepared using a one-step hydrothermal process with different reaction times. The results showed that the $H_2V_3O_8$ nanorods with a 36 h reaction time presented a better electrochemical performance.

Furthermore, the $H_2V_3O_8$/MXene composites were similarly synthesized. It was demonstrated that such favorable morphology and structure with 1D nanorod-like $H_2V_3O_8$, as well as 2D lamellar MXene materials, were beneficial for accelerating the ion migration rate, and provided more active sites for the insertion and removal of zinc ions. As a result, the $H_2V_3O_8$/MXene composites promoted the rate capability, cycle stability and specific discharge capacity, when compared with using $H_2V_3O_8$ nanorods as the cathode. The initial specific discharge capacity reached 373 mA h g^{-1} at 200 mA g^{-1} and it had only 15.8% capacity attenuation at 500 mA g^{-1} after 5000 cycles. Therefore, the results provide an alternative strategy for the development of new energy storage batteries.

Conflicts of interest

There are no conflicts to declare.

Acknowledgements

This research was supported by the Natural Science Foundation of Shaanxi Province (Grant No. 2023-JC-QN-0615), the Natural Science Foundation of Shaanxi Provincial Education Department (Grant No. 22JK0595) and the Scientific Research Fund for the High-level Talents of Xijing University (Grant No. XJ22B10).

Notes and references

1 V. Verma, S. Kumar, W. Manalastas Jr, R. Satish and M. Srinivasan, *Adv. Sustainable Syst.*, 2019, **3**, 1800111.
2 A. Rahil, E. Partenie, M. Bowkett, M. H. Nazir and M. M. Hussain, *Battery Energy*, 2022, **1**, 20210001.
3 Y. Song, T. Wang, J. Zhu, Y. Liu, L. Wang, L. Dai and Z. He, *J. Alloys Compd.*, 2022, **897**, 163065–163078.
4 D. Kornilov, T. R. Penki, A. Cheglakov and D. Aurbach, *Battery Energy*, 2022, **1**, 20210002.
5 H. Zhang, L. Wang and X. He, *Battery Energy*, 2022, **1**, 20210011.
6 Y. Guo, Y. Zhang and H. Lu, *Battery Energy*, 2022, **1**, 20210014.
7 Y. Ma, M. Wu, X. Jin, R. Shu, C. Hu, T. Xu, J. Li, X. Meng and X. Cao, *Chem. – Eur. J.*, 2021, **27**, 12341–12351.
8 G. He, Y. Liu, D. E. Gray and J. Othon, *Compos. Commun.*, 2021, **27**, 100882.
9 X. Dong, Y. Mu, L. Shen, H. Wang, C. Huang, C. Meng and Y. Zhang, *Chem. Eng. J.*, 2023, **456**, 141031.
10 J. Chen, J. Ma, B. Liu, Z. Li, X. Zhang, S. Sun, K. Lu, J. Yin, S. Chen, X. Zu, Z. Zhang, X. Qiu, Y. Qin and W. Zhang, *Compos. Commun.*, 2023, **38**, 101524.
11 Q. Yin, L. Chen, Y. Chen and F. Zhan, *Compos. Commun.*, 2021, **26**, 100728.
12 Y. Lyu, J. Yuwono, P. Wang, Y. Wang, F. Yang, S. Liu, S. Zhang, B. Wang, K. Davey, J. Mao and Z. Guo, *Angew. Chem., Int. Ed.*, 2023, e202303011, DOI: **10.1002/anie.202303011**.
13 A. Qian, Y. Pang, G. Wang, Y. Hao, Y. Liu, H. Shi, C.-H. Chung, Z. Du and F. Cheng, *ACS Appl. Mater. Interfaces*, 2020, **12**, 54791–54797.
14 X. Li, M. Li, Q. Yang, G. Liang, Z. Huang, L. Ma, D. Wang, F. Mo, B. Dong, Q. Huang and C. Zhi, *Adv. Energy Mater.*, 2020, **10**, 2001791.
15 X. Wang, Y. Wang, J. Hao, Y. Liu, H. Xiao, Y. Ma, L. Chen, Y. Huang and G. Yuan, *Energy Storage Mater.*, 2022, **50**, 454–463.
16 C. Liu, W. Xu, C. Mei, M.-C. Li, X. Xu and Q. Wu, Highly stable $H_2V_3O_8$/Mxene cathode for Zn-ion batteries with superior rate performance and long lifespan, *Chem. Eng. J.*, 2021, **405**, 126737.
17 A. Mateen, M. Z. Ansari, I. Hussain, S. M. Eldin, M. D. Albaqami, A. A. A. Bahajjaj, M. S. Javed and K.-Q. Peng, *Compos. Commun.*, 2023, **38**, 101493.
18 P. He, Y. Quan, X. Xu, M. Yan, W. Yang, Q. An, L. He and L. Mai, *Small*, 2017, **13**, 1702551.
19 M. Rastgoo-Deylami, M. S. Chae and S.-T. Hong, *Chem. Mater.*, 2018, **30**, 7464–7472.
20 D. Wang, Q. Wei, J. Sheng, P. Hu, M. Yan, R. Sun, X. Xu, Q. An and L. Mai, *Phys. Chem. Chem. Phys.*, 2016, **18**, 12074–12079.
21 H. Tang, N. Xu, C. Pei, F. Xiong, S. Tan, W. Luo, Q. An and L. Mai, *ACS Appl. Mater. Interfaces*, 2017, **9**, 28667–28673.
22 D. Chen, X. Rui, Q. Zhang, H. Geng, L. Gan, W. Zhang, C. Li, S. Huang and Y. Yu, *Nano Energy*, 2019, **60**, 171–178.
23 X. Zhu, Z. Cao, X.-L. Li, L. Pei, J. Jones, Y.-N. Zhou, P. Dong, L. Wang, M. Xe and J. Shen, *Energy Storage Mater.*, 2022, **45**, 568–577.
24 M. Mahmood, S. Zulfiqar, M. F. Warsi, M. Aadil, I. Shakir, S. Haider, P. O. Agboola and M. Shahid, *Ceram. Int.*, 2022, **48**, 2345–2354.
25 N. Zhang, L. Qiu, X. Liu, P.-F. Wang, Y.-R. Zhu and T.-F. Yi, *Ceram. Int.*, 2023, **49**, 17668–17679.
26 J. Chen, M. Chen, W. Zhou, X. Xu, B. Liu, W. Zhang and C. Wong, *ACS Nano*, 2022, **16**, 2461–2470.
27 M. Chen, J. Chen, W. Zhou, X. Han, Y. Yao and C.-P. Wong, *Adv. Mater.*, 2021, **33**, 2007559.
28 Y. Li and B. Wang, *Battery Energy*, 2023, **2**, 20220035.
29 Y. Liu, P. A. Russo, L. A. Montoro and N. Pinna, *Battery Energy*, 2023, **2**, 20220037.
30 J. W. Kim, J. L. Digol, S. Bong and J. Lee, *Battery Energy*, 2023, **2**, 20220024.
31 W. Li, J. Li, R. Li, X. Li, J. Gao, S.-M. Hao and W. Zhou, *Battery Energy*, 2023, **2**, 20220042.
32 R. Xu, N. Sun, H. Zhou, X. Chang, R. A. Soomro and B. Xu, *Battery Energy*, 2023, **2**, 20220054.
33 B. Zhang, L. Wang, H. Zhang, H. Xu and X. He, *Battery Energy*, 2022, **1**, 20220020.
34 S. Wang, W. Deng, Z. Geng, P. Li, N. Hu, L. Zhu, W. Sun and C. M. Li, *Battery Energy*, 2023, **2**, 20220050.
35 Z. Li and A. W. Robertson, *Battery Energy*, 2023, **2**, 20220029.
36 Z. Xing, B. Wang, J. K. Halsted, R. Subashchandrabose, W. F. Stickle and X. Ji, *Chem. Commun.*, 2015, **51**, 1969–1971.
37 L. Cheng, C. Ma, W. Lu, X. Wang, H. Yue, D. Zhang and Z. Xing, *Chem. Eng. J.*, 2022, **433**, 133527.
38 W. Li, D. Peng, W. Huang, X. Zhang, Z. Hou, W. Zhang, B. Lin and Z. Xing, *Carbon*, 2023, **204**, 315–324.